Journal of Alloys and Compounds 488 (2009) 181–189

Contents lists available at ScienceDirect

Journal of Alloys and Compounds

journal homepage: www.elsevier.com/locate/jallcom

Electron-backscattered diffraction and transmission electron microscopy study of post-creep Ti_3SiC_2

F. Barcelo[a], S. Doriot[a], T. Cozzika[a], M. Le Flem[a], J.L. Béchade[a], M. Radovic[b,*], M.W. Barsoum[c]

[a] CEA/DEN - Section for Applied Metallurgy Research 91191 Gif Sur Yvette, France
[b] Department of Mechanical Engineering, Texas A&M University, College Station, TX 77840, USA
[c] Department of Materials Science and Engineering, Drexel University, Philadelphia, PA 19104, USA

ARTICLE INFO

Article history:
Received 28 March 2009
Received in revised form 14 August 2009
Accepted 17 August 2009
Available online 25 August 2009

Keywords:
Carbides
Creep
Electron backscatter diffraction
Transmission electron microscopy

ABSTRACT

The post-creep microstructures of coarse-grained (100–200 μm) and fine-grained (3–5 μm) Ti_3SiC_2 samples – both loaded in air at 1000 °C, under a tensile stress of 80 MPa were studied by electron backscatter diffraction, EBSD, and transmission electron microscope, TEM. The CG sample ruptured after ≈100 h, with a strain to failure of ≈2.5% that was mostly concentrated near the fracture plane. Analysis of more than 35 grains in the undeformed grip area indicated that the maximum misorientation, MO, angle within each grain was <2°. In the deformed area, roughly 1.2 mm below the fracture surface, the MO's – again within *each* grain – varied dramatically; in some grains, MO's of the order of 10° in narrow spatial range – attributed to kink boundaries – were observed; in others, the MO was <2°, i.e. they were un-deformed. Further analysis of the grains with large MO's revealed two types of deformed grains. Ones in which the kink boundaries – responsible for the MO – alternated in angle, or sign, forming a herring-bone like structure, and others in which they were all in same direction, causing bending of the basal planes. The latter deformation mechanism was confirmed by TEM. The TEM, on both fine and coarse-grained samples revealed the presence of dislocation arrays, low angle grain boundaries, as well as triple point cavities.

1. Introduction

Since fully dense single-phase bulk samples of Ti_3SiC_2 were first synthesized [1], it has been established that this compound, exhibits an unusual combination of properties [1–13] such as high specific stiffness, with ease of machinability [1,7], excellent thermal and electrical conductivities [14], as well as, exceptional damage, thermal shock [1,9], oxidation [11,15] and fatigue resistance [4,16]. At room temperature, favorably oriented microstructures exhibit ductile behavior[8].

The mechanical response of Ti_3SiC_2 – and by extension all other $M_{n+1}AX_n$ phases [7,13,17], where M is a transition metal, A is an A group element and X is carbon and/or nitrogen – can be traced to their high c/a ratios that render them extremely plastically anisotropic because they eliminate the possibility for non-basal dislocations. Their response to stress can thus be traced to three facts: (i) basal slip, and only basal slip, is operative at all temperatures [5,6] – no other dislocations but perfect, mixed, basal plane dislocations are observed in transmission electron microscope, TEM, micrographs [5,6,18]; (ii) twins, apart from basal, – viz. $\{1\,1\,\bar{2}\,1\}$, which are a special case of kinking that can form by dislocation glide [19] – are unlikely, and have never been observed. Instead, deformation occurs by a combination of glide and formation of kink bands, as well as delaminations within individual grains [20]; (iii) because they are confined to the basal planes, the dislocations arrange themselves either in arrays (pileups) on the same slip plane, or in walls (low- or high-angle grain boundaries) normal to the arrays [6]. Thus, at no time are the five independent slip systems required for ductility operative and at no time do the dislocations entangle to form forests; the only possible interaction is orthogonal, where the pileups and the walls intersect [6].

Recently, we showed that macroscopic polycrystalline Ti_3SiC_2 cylinders can be compressed, at room temperature, to stresses up to 1 GPa, and fully recover upon the removal of the load [2]. This phenomenon was attributed to the formation and annihilation of fully reversible, incipient kink bands, IKBs, defined as parallel dislocation loops in basal planes (top left inset, Fig. 1), wherein the edge dislocation segments are of opposite polarity, that remain attached, and are thus attracted to each other [21]. Removal of the load allows the IKBs to collapse and shrink significantly and/or be eliminated. And while no direct evidence for IKBs has been obtained to date, the circumstantial evidence, together with a recent microscale model, which is in excellent agreement with experimental results, leave little doubt to their existence [22–24].

* Corresponding author. Tel.: +1 979 845 5114.
E-mail address: mradovic@tamu.edu (M. Radovic).

0925-8388/$ – see front matter © 2009 Elsevier B.V. All rights reserved.
doi:10.1016/j.jallcom.2009.08.073

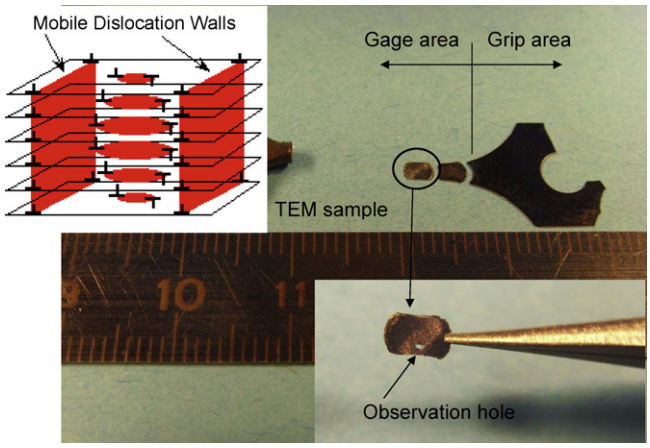

Fig. 1. Two halves of a dog-bone, fine-grained sample after creep testing. The half of the sample, shown on the right, was sliced into a thin foil. Bottom inset shows TEM sample cut from the gage area. Top left inset is a schematic of an IKB; removal of the load results in its shrinkage or elimination. In this schematic, the ends of the IKB in the center, are sundered, resulting in mobile dislocation walls.

At temperatures higher than ≈1000 °C, the mutual attraction holding the IKB dislocations together weakens, most probably because of a weakening of the grain boundary cohesive strengths and/or ease of delamination [3]. The weakening in turn results in the devolution of the IKBs into parallel, mobile dislocation walls, MDW (top left inset, Fig. 1). Once detached, the walls are mobile until they encounter an obstacle, such as a grain boundary or another wall [2]. Furthermore, once the walls separate some distance, other IKBs can nucleate within the area between them, in turn forming new MDWs, etc. It is the coalescence of these MDW, from the same or adjacent sources, that results in the formation of kink boundaries [6,8,25]. Said otherwise, large grains are broken into smaller ones, which, in turn, results in cyclic hardening at both the creep temperatures and after cooling to room temperature [2,26].

Another major consequence of this plastic anisotropy is the development of large internal stresses in grains that are not favorably oriented to the applied stress – so called hard grains. Like in ice, with which it shares many commonalities [27], the mechanical response of the MAX phases is dictated by a competition between the rates at which the internal stresses accumulate versus the rates at which they can be relaxed. This uneven distribution of stresses also renders the deformation quite strain rate sensitive and strain rate exponents of 0.5 are typical [28–30]. If loaded rapidly, fracture occurs readily; if loaded slowly, however, they can be quite plastic [27].

In both tension and compression we have shown that up to strain of ≈4%, the deformation is accommodated by plastic deformation with *little* cavitation; beyond that strain intensive cavitation is observed [26,28–30]. The strain distribution, however, can be quite non-uniform, especially when the samples are loaded rapidly. At higher stresses and/or temperatures that deformation is confined to a region near the fracture plane [26,28–30].

Although significant progress has been achieved in understanding the mechanical behavior of Ti_3SiC_2 as a function of temperature and grain size, as far as we are aware there have been no reports in which the post-tensile, or any, creep microstructures have been studied in detail to confirm the microstructural evolution surmised from their mechanical behavior, i.e. from the stress–strain curves.

The purpose of this paper is to report on the results of a transmission electron microscopy, TEM, and electron-backscattered diffraction, EBSD, studies of both, coarse- and fine-grained Ti_3SiC_2 samples that were crept in tension at 1000 °C.

Table 1
Summary of grain sizes and creep conditions. Also listed are the times to rupture and strains to failure. Both samples were subjected to a tensile stress of 80 MPa at 1000 °C.

	Grain size		Time to rupture (h)	Strain to failure (%)	Ref.
	Diameter	Thickness			
Coarse	42 ± 39	20 ± 16	≈110	2.5	[29]
Fine	8 ± 4[a]	3 ± 1.5[a]	≈42	≈2.0	[28]

[a] Reported in Ref. [29].

2. Experimental details

The details of the creep experiments can be found elsewhere [28,29]. In short, tensile dog-bone samples – with 2.5 × 2.5 × 12 mm^3 gage area – were loaded in air and the strain was measured as a function of time using a laser extensometer. Table 1 summarizes the initial microstructures and creep conditions of the two samples – one coarse-grained, CG, and the other fine-grained, FG – studied in this work.

Because grain growth in Ti_3SiC_2 is anisotropic – with growth along the *a*-axis being faster than along the *c*-axis [10] – the grains are not equiaxed, but tend to grow as hexagonal plates, with a diameter that can be larger than their thickness along the [0 0 0 1] direction (Table 1). Another consequence is that the grain size distribution for the CG material tends to be quite wide, wherein significantly smaller grains can be found in between the larger ones (Fig. 2). The grains in the FG samples tend to be more equiaxed, with a narrower grain-size distribution (Table 1).

The EBSD measurements were performed using JEOL JSM 6400 scanning electron microscope, SEM, with LaB_6 filament. The samples were ground, and polished with a diamond suspension with particle size from 9 μm down to 1 μm. Experimental analyses were carried out at acceleration voltage of 20 kV, working distance of 25 mm and using diaphragm no. 2, and with a sample tilted 70° to horizontal. EBSD maps were acquired and processed at 2 μm step with an integration time of 0.12 ms per point using Channel 5 software in a HKL Technology local orientation system. Indexation was performed from Kikuchi bands, using 61 reflection planes and 10 bands in Hough space resolution. An arithmetic average of four acquisitions was determined for each point of EBSD analysis maps.

In order to prepare the TEM samples, roughly one half of both, coarse- and fine-grained dog-bone shaped samples were sliced into thin foils after they had failed in creep. Fig. 1 shows two halves of the FG sample, one of which – shown on the right – was sliced into a thin foil. Two TEM samples (Fig. 1) were cut from the deformed gage and undeformed grip areas of the FG and GC samples. The TEM specimens were then thinned to ~70 μm by diamond polishing plus a final polishing with alumina suspension to avoid preparation strips. An observation hole was introduced by ion milling (Ion Tech Ion Miller) operating at 5 kV. The samples were examined using a TEM (JEOL FEG STEM 2010 F).

3. Results

3.1. EBSD of coarse-grained samples

A typical SEM micrograph of grains in the gauge area is shown in Fig. 2a. The corresponding OIM pattern of the region within the rectangular frame in Fig. 2a is shown in Fig. 2b. The corresponding rainbow pattern of the same area (Fig. 2c) shows that the misorientations in grain I were <2°, while those in grain II were between 0° and 8° (see below). The pole figures for grains I and II are shown in 2d. Note that in grain II, in which line labeled C appears, the basal planes are edge-on.

Analysis of more than 35 grains in the un-deformed grip area indicated that the misorientation, MO, angle – within *each* grain – was at *most* 2°; in many cases it was <1°. A typical trace of the MO angle along a large grain in the grip area is shown in Fig. 3 (squares). Fig. 3 also shows the trace of the MO angle along line A (open circles) in Fig. 2b, indicating that very little deformation was experienced by this part of the grain. Conversely, a trace along line B in Fig. 2b – also shown in Fig. 3 – indicates a narrow region in which the MO angle increases abruptly and sharply up to ≈8° (open diamonds).

A trace of the MO angle along line C in Fig. 2b, yields a more complicated structure, where the MO angle fluctuates between 0° and 8° (Fig. 4a). Here again, based on the unit cells orientations,

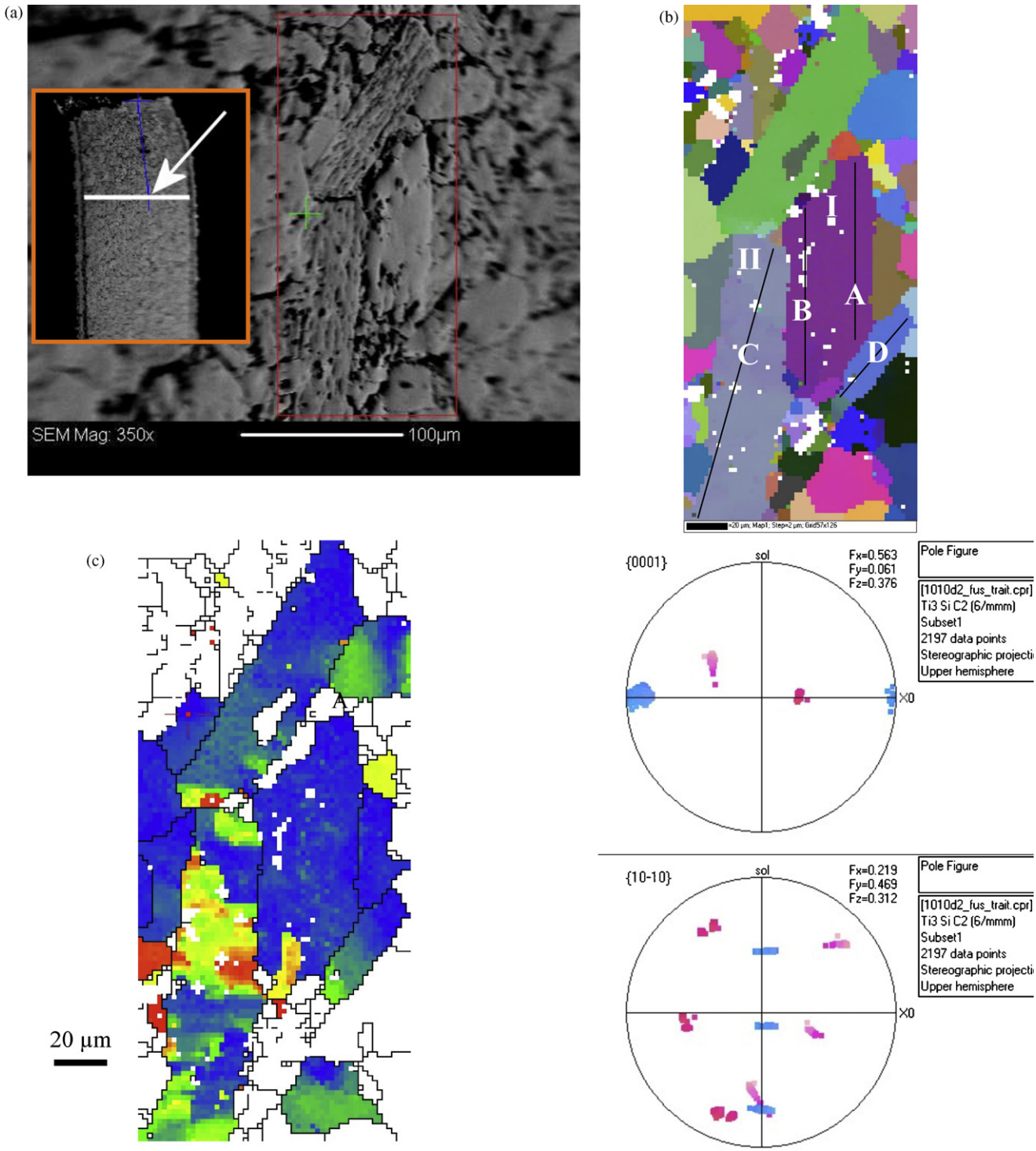

Fig. 2. (a) Backscattered SEM micrograph of gauge area. Inset shows a low magnification SEM micrograph of entire sample. The OIM information was taken at the location, denoted by the white horizontal line, that was ≈1.5 mm below the fracture plane, which is at the top of the figure. Width of sample is 2 mm. Applied load is in the vertical direction. (b) OIM of area bounded by red rectangle in a; (c) Individual MO angle map within *each* grain, with blue MO = 0° and red MO = 10°. (d) Pole figures for grains I and II in Fig. 2b. Note that in grain II, in which line labeled C appears, the basal planes are edge-on. (For interpretation of the references to color in this figure legend, the reader is referred to the web version of the article.)

shown in Fig. 4a, and the spatial rainbow map of the MO of the same grain (Fig. 2c), it is reasonable to infer the existence of four regions with the same crystal orientation. Based on the orientations of the unit cells on each side of the transition in Fig. 4a that clearly show the MO to be due to a ≈8° tilt, we conclude that the transition occurs at a kink boundary. A schematic of the multi-kinking grain, reminiscent of an "accordion", is shown in lower left inset in Fig. 4a. Note, that since the basal planes are parallel to the A direction, it follows that kinking occurred in a direction that is almost *parallel* to the vertically applied tensile stresses.

Coincidentally or not, the MO of a $\{1\,1\,\bar{2}\,1\}$ twin relative to the basal planes should be 9.7°. As noted above, in the MAX phases and other KNE solids, $\{1\,1\,\bar{2}\,1\}$ twins are nothing but special kink boundaries, where a dislocation is found every *c*-lattice parameter [19].

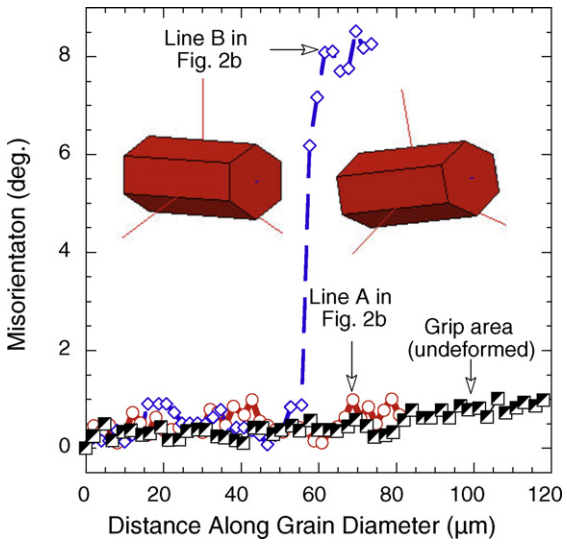

Fig. 3. Traces of MO angle along an undeformed large grain (in the grip area) and along lines A and B of the large deformed grain labeled I in Fig. 2b. Unit cells, shown as insets, denote orientation of planes on either side of the kink boundary with respect to the direction of the vertically applied load.

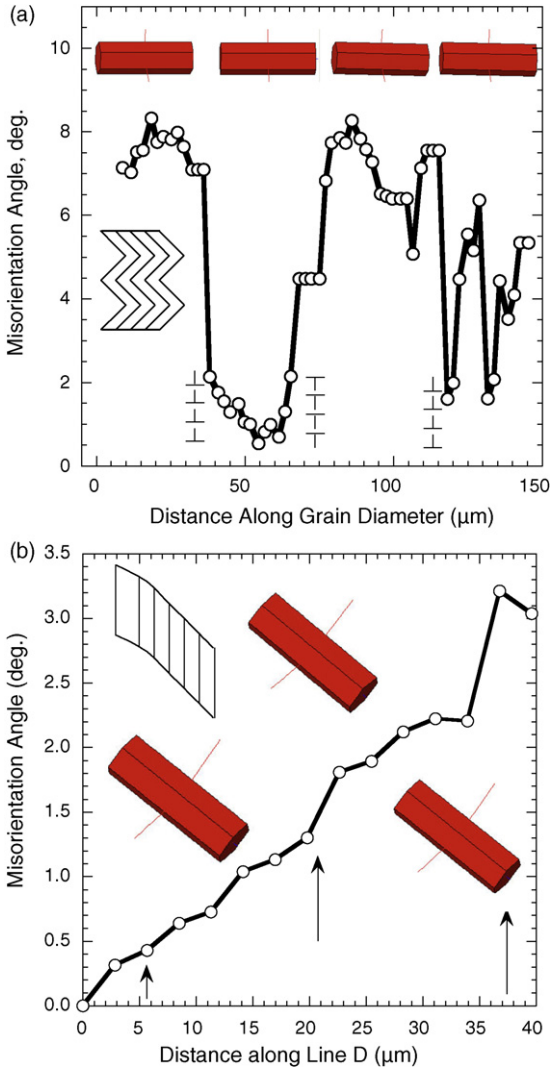

Fig. 4. Traces of MO angle in deformed grain (a) for grain II along line C in Fig. 2b, (b) for grain III along line D, shown in Fig. 2b. Unit cells in a and b, denote their orientation with respect to the direction of vertically applied load.

For angles >9.7°, a dislocation must exist at an average distance < *c*, as was previously observed [5].

A trace of MO angle along line D in grain III – shown in Fig. 2b – yields a different response (Fig. 4b). Here the MO angle changes gradually from one side of the grain to the other and has a maximum value of ~3.4°. Note that this gradual change in angle is unlikely to be due to a defocalisation, resulting from the sample's tilted position.

Attempts to identify kink boundaries, bent grains, etc., in the fine-grained microstructure by EBSD were unsuccessful. It is not clear at this stage whether that is because they do not exist or because they are below the detectability limit of our equipment.

3.2. TEM of coarse-grained samples

TEM micrographs of the undeformed grip area revealed few dislocation arrays in the grains (Fig. 5a) and some dislocations in the grain boundaries. The examined grip area was fully dense; no pores or cavities were observed. Note that due to the relatively large size of the grains, only a few grains were observable in a given TEM sample.

TEM of the deformed gauge area revealed a more complex microstructure with evidence of inhomogeneous deformation. After creep, the deformation was quite heterogeneous; some grains have a high density of dislocations (Fig. 5b and c); others had low dislocation densities that were comparable to the as-sintered samples (not shown here). Fig. 5d shows an array of stacking faults that are more or less homogeneously distributed inside the grains of the undeformed grip area. Also seen on the same figure (white arrows) are dislocation walls. In other grains, narrow bands, with high densities of defects (Fig. 5e and f), were also seen. In contrast to stacking faults, that are more or less uniformly distributed, these bands are unique and compact and most probably correspond to shear bands. It is worth noting, that such highly localized shear bands in the deformation area were not seen before the creep tests, where only uniform stacking faults were observed. The average dislocation density of 15×10^6 m/m^2 estimated in the gauge area (Fig. 5b) is significantly larger than the dislocation density of 0.75×10^6 m/m^2 in grip area (Fig. 5a).

As previously observed by optical microscopy on the same samples [29], and unlike the as-sintered undeformed samples, grain boundary steps were observed in post-creep samples. The beginning of a step formation is shown for a CG sample in Fig. 5c. These steps were numerous, can be wide – up to 1 μm – and were never observed in non-deformed samples. The steps – labeled with vertical arrows in Fig. 5c are most probably a result of basal dislocation glide and also seem to be the source of dislocations arrays (horizontal arrows in Fig. 5c) in the grain to the right of the boundary.

Although, it can be argued here that the observed plastic deformation originate from the loads applied during processing, as noted above, several microstructural features indicate that the majority of the plastic deformation observed in the gage area resulted from the high temperature creep.

Unlike in the undeformed grip area, TEM of the gage area showed the presence of a few polygonal cavities (not shown) that were probably formed during sintering or due to the pull out of inclusions during specimen preparation. In addition, some non-polygonal cavities, most probably formed as a result of the deformation of surrounding grains, were also observed.

The most remarkable result of the TEM study is shown in Fig. 6a and b. A high magnification image (Fig. 6b) of the area between the two near parallel dislocation arrays clearly shows the bending of the basal planes. From Fig. 6b, the radius of curvature of these planes is estimated to be ~900 nm.

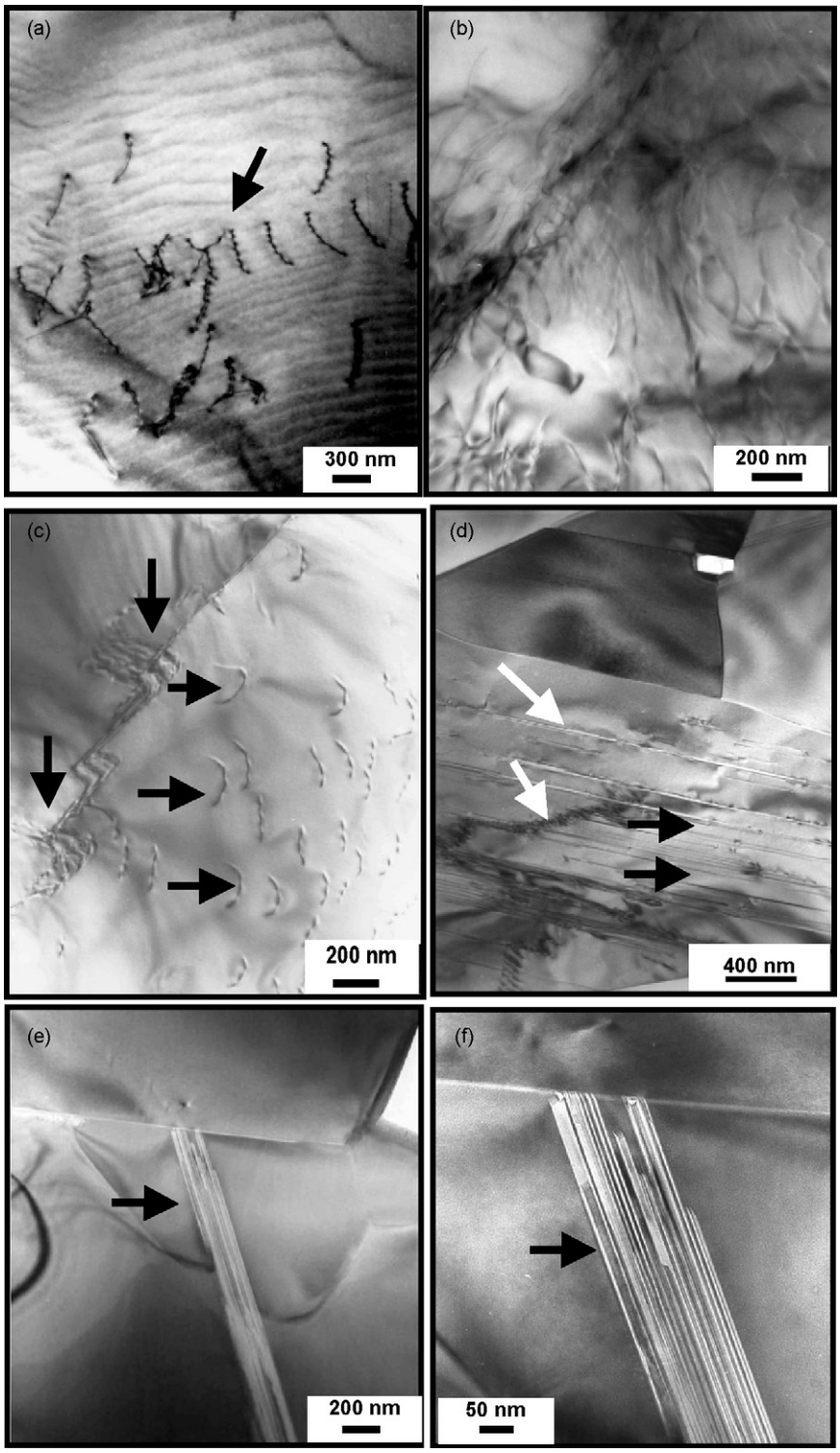

Fig. 5. TEM micrographs of coarse-grained sample. (a) Dislocation arrays (denoted by arrow) in un-deformed grip area, (b) large number of dislocations in a highly deformed grain, (c) grain boundary steps (vertical arrows) and dislocation arrays (horizontal arrows) after creep test, (d) high density of basal stacking faults (black arrows) and low angle grain boundaries (white arrows) in undeformed grip area, (e) shear band in deformed region and (f) same as e, but at higher magnification.

3.3. TEM of fine-grained samples

The microstructure of the undeformed FG sample (not shown) consisted mostly of plate-like grains, with numerous basal plane dislocations, stacking faults and very few cavities. The few cavities observed could be attributed to either incomplete densification during fabrication and/or pullouts of secondary phases, most commonly TiC, during sample preparation. It is non-trivial to fabricate Ti_3SiC_2 with no TiC_x, especially the FG microstructure. The sample tested here had ≈2 vol.% TiC.

After deformation a large number of triangular cavities, located mostly at triple points, were observed. As denoted in Fig. 7a, by white arrows, the cavities are uniformly distributed and their size ranges from ∼50 nm to more than ∼500 nm. Only few grains with

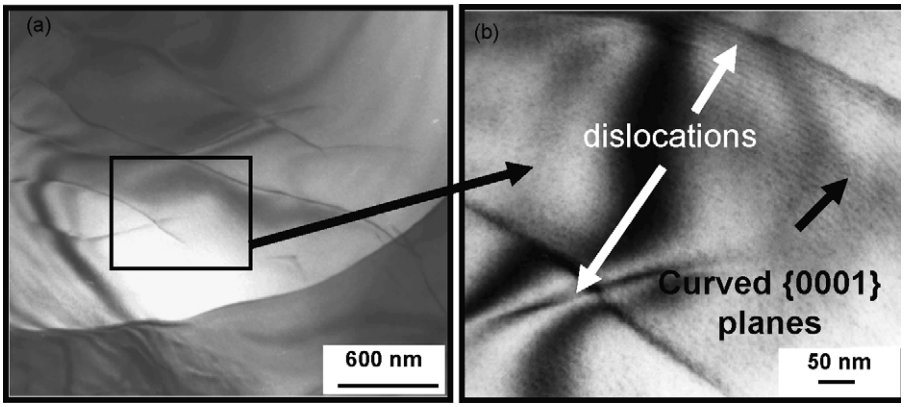

Fig. 6. TEM micrograph of deformed gauge area of CG sample at, (a) low magnification and (b) higher magnification. Note severe bending of basal planes between two dislocation arrays denoted by white arrows.

basal plane dislocation arrays – one of them denoted by a thick black arrow in Fig. 7a – were seen in the grains surrounding the cavities.

In this case, the dislocation density after creep was apparently *lower* than in the grip area. Some stalking faults, that probably existed before deformation – denoted by black arrows on Fig. 7 – were also seen. Similar to the grain boundary steps observed in the GC samples, here again similar steps were frequently observed (Fig. 7b). Such steps were never observed in the as-sintered, undeformed sample.

As in the case of the CG sample, grain boundary steps (Fig. 7b) were frequently observed. Here again, these steps were most likely formed by the glide of basal plane dislocations in favorably oriented grains. The white arrows in Fig. 7b mark triangular cavities that were formed at the grain boundaries.

Fig. 8a shows a low angle boundary, A–B, located between areas A and B. Basal planes were observed in both areas. The specimen is positioned in such a way that the basal planes of area A are close to being edge-on (inset of Fig. 8a). A step, labeled 1 in Fig. 8a, can be observed along the A–B boundary. This step, shown in Fig. 8a and d, is probably formed as a result of dislocation glide along basal planes in area A. To accommodate this step, the basal planes in area B are highly deformed, i.e. bent (Fig. 8d labeled 2), in a manner similar to that was observed in CG sample (Fig. 6b). At ~220 nm, however, the radius of curvature of the basal planes in area B is significantly smaller than the ones measured in the CG structure. Furthermore, the crystal structure in area B – marked by arrow 3 in Fig. 8a and d, and magnified in Fig. 8e – is very disturbed in the vicinity of the step. This indicates that further deformation would have probably resulted in decohesion and cavitation at the step edge. Fig. 8b and c show magnified images of dislocation arrays or stacking faults labeled 4 in Fig. 8a. Note that the stacking fault/array does not appear to be associated with, and/or an extension of, the low angle grain boundary step.

It is not clear at this point if areas A and B (Fig. 8a) are two separate grains, or subgrains that were formed as a result of creep. The projection of basal planes in areas A and B are obviously not parallel, as it can be observed along A–B in Fig. 8a. However, careful observation of the micrograph shown in Fig. 8d leads to the conclusion that projections of basal planes in areas A and B become almost parallel at the tip of the area with the disturbed microstructure, i.e. above in the area labeled 2 in Fig. 8d, i.e. at the top right corner in Fig. 8a. It thus seems that the basal planes in area B bend to accommodate the formation of the step in the low angle boundary. It follows that the latter most probably formed as a result of the plastic deformation of the sample.

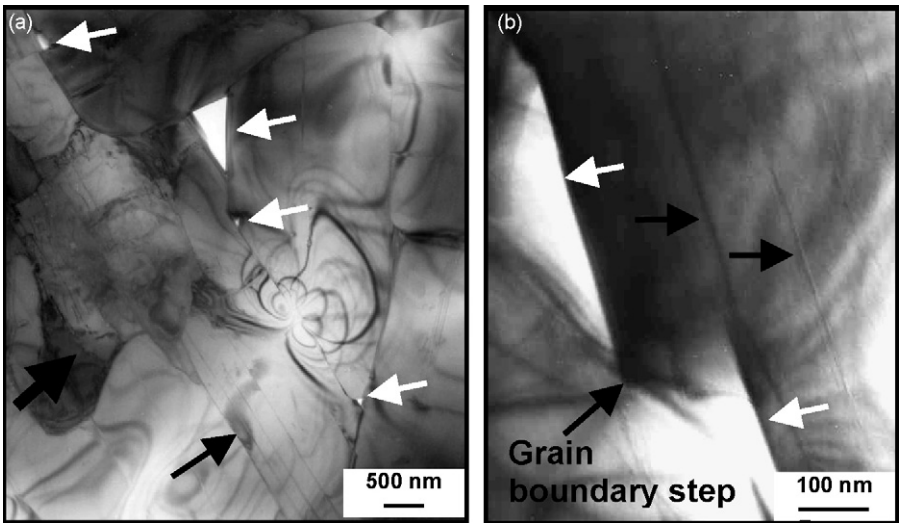

Fig. 7. Post-creep TEM micrograph of FG sample showing. (a) Triangular cavities (white arrows), grains with dislocations (thick black arrow) and stacking faults or dislocation arrays (thin black arrow) and (b) triangular cavities (white arrows), grain boundary steps and dislocation arrays and/or stacking faults (black arrow).

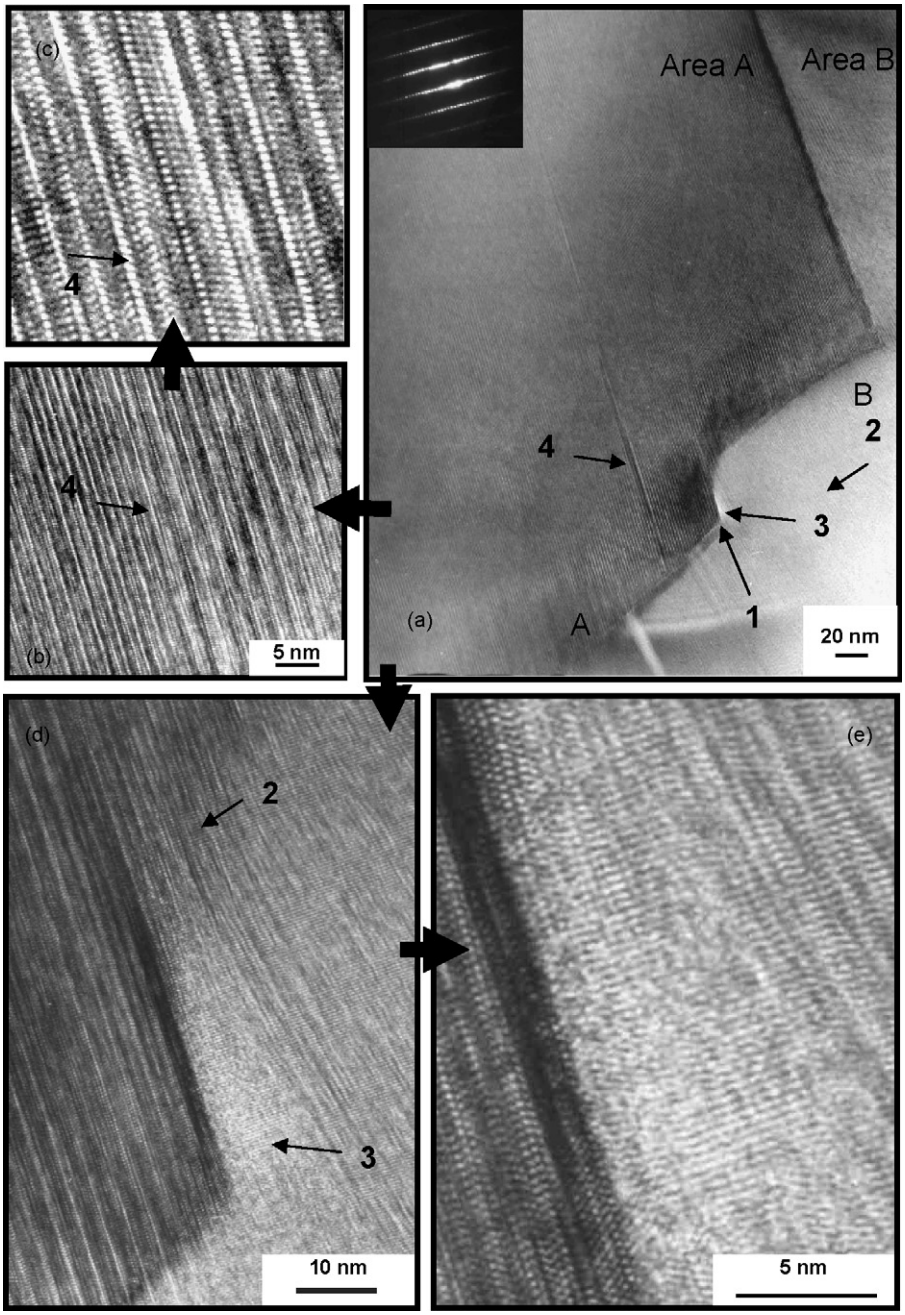

Fig. 8. TEM micrograph of two areas, A and B, separated by the A–B low angle boundary. (a) General view showing—1: step in low angle boundary, 2: bent basal planes near the step, 3: disturbed crystal structure, and 4: stalking fault. Inset shows selected area diffraction pattern of area 1; (b) and (c) magnified images of stacking fault labeled 4 in a; (d) and (e) magnified area near edge of boundary step labeled with 2 and 3 in a.

4. Discussion

Based on the totality of the results shown herein, it is clear that, as previously surmised [28–31] the tensile creep strain results from a combination of (a) cavity formation and (b) plastic deformation of individual grains. The EBSD and TEM results suggest at least three different deformation mechanisms of individual grains, namely: (i) basal dislocation glide to form dislocation arrays/stacking faults (ii) formation of dislocation walls of opposite sign that result in kinking of individual grains (Fig. 4a), and (iii) formation of mobile dislocation walls, MDW, or low angle grain boundaries of the *same* sign that result in grain bending (Figs. b and Fig. 8). The latter mechanism results in polygonized grains. Note the distinction between low angle grain boundaries and MDWs is made here only to be consistent with the literature; they are synonymous.

The extreme plastic anisotropy of Ti_3SiC_2, insures that, like in other plastically anisotropic solids, such as ice [27], highly non-uniform local stress distributions are common. The latter is manifested in the non-homogeneous deformation found in EBSD analyses, which revealed the existence of non-deformed grains together with banana-shaped and kinked grains (Figs. 2–4). In one example, parts of the *same* grain apparently experienced quite different deformations. For example, along line A of grain I in Fig. 2a, there was no MO (Fig. 3a) and presumably no deformation; along line B, which lies in the same grain, however, a KB was observed (Fig. 3a).

The most dramatic illustration of the complex relationship between kinking and the state of non-uniform stresses is shown in Fig. 4a. Grain II, kinked like an accordion along the *axial* direction, despite the fact that the sample was loaded in *tension in the same direction*! This is a remarkable result that is not easily reconciled with strain energy considerations or common sense. Intuitively, one would expect grains, whose basal planes are *perpendicular* to the applied load, to kink in tension; the opposite being true in compression. The simplest explanation has to be that dislocation pileups in adjacent grains caused the grains shown in Fig. 4a and b, to kink the way they do. This comment notwithstanding it is hereby acknowledged that more work is needed to better understand this unexpected – that was not isolated, but quite common – observation.

It is important to note that a somewhat similar observation was made, decades ago, by Hauser et al. [32], who studied the deformation of CG Mg. In that paper they showed that in one specimen 10 twins caused extension and 23 caused contraction in the stress direction. Hauser et al. [32] concluded, "... the overall strain due to twinning in this specimen is actually *negative*, a fact *not* easily reconciled with strain energy considerations". The similarities between Ti_3SiC_2 and Mg run deeper than this commonality. Very recently we showed that several hexagonal metals, including Mg, Co, Zn and Ti, are like the MAX phases KNE solids [24,33]. It is thus not surprising that they behave similarly. Along those lines it is important to note that in an EBSD study of post-creep CG Mg subjected to tensile stresses – very reminiscent of this work – the central and key role of kink boundaries in the deformation process was clearly and unambiguously proven [34].

Not surprisingly, the numerous TEM micrographs shown herein confirm the EBSD conclusions and those of previous work [28,31]: dislocations glide on basal planes during the high-temperature creep of both FG and CG Ti_3SiC_2. Fig. 5c, shows dislocation pileups (arrays) that formed on grain boundaries in the CG structure, while Fig. 5e and f shows shear bands that formed, presumably also as a result of dislocation glide. In the FG samples evidence for dislocation glide is also numerous (Fig. 7b). When deformation of a grain induced by glide of basal plane dislocations in favorably oriented grains cannot be accommodated by the deformation of adjacent grains, steps and triangular cavities form at the grain boundaries as shown in Fig. 7b. Both, glide and basal dislocations pileups, as well as the formation of grain boundary steps and cavities were observed by TEM and SEM in earlier work in samples deformed at room and high temperatures in static tests [6,29].

Certainly, the most intriguing feature observed in both microstructures is the extreme bending of the basal planes observed in some grains (Figs. Fig. 6b and Fig. 8d). And while it may be argued – as apparent in the micrographs – that the basal planes are bent elastically, conservative calculations carried out in Appendix A, suggest that tensile stresses >20 GPa, and shear stresses >15 GPa, would be required to sustain them. Since such stresses are clearly impossible, it is reasonable to conclude that the observed bending must be due dislocations that we cannot image. Furthermore given that we do not observe low angle grain boundaries or what we call mobile dislocation walls – that are readily observable in this material as we have shown previously shown [5,6] – then the most likely explanation is that the dislocations causing the curvature are *diffuse* and thus not readily observable. Needless to add, the evidence for such parallel dislocation walls of the same sign is clearly visible in the EBSD results (Fig. 4b). These comments notwithstanding, clearly more work is needed to fully understand this extreme bending.

Lastly, a few differences in the post-creep structures of the FG and CG samples need to be emphasized. Although, a relatively small number of the grains were studied by TEM, the deformation in the FG structure seems to be more homogeneous than in the CG structure. In the FG samples, deformation seems to occur predominately by basal slip leading to steps at grain boundaries and cavitations at the edges of these steps and bending of the basal planes as a result of MDWs or low angle grain boundaries. The fact that the dislocation density in the gauge area of FG samples, after deformation, appears to be *lower*, than in the grip section, suggests the presence of an effective dislocation annihilation mechanism the most likely being the grain boundaries. Another possibility is the nucleation of cavities that cause stress relaxation and the concomitant annihilation of dislocations. These comments notwithstanding, it is hereby acknowledged that we need to emphasise that this is a tentative conclusion and more comprehensive TEM work on other samples deformed under different conditions need to be examined.

In the CG sample, deformation is more complex, wherein basal slip leads to the formation of kink bands and parallel dislocation walls. The deformation is also quite non-homogeneous. In the CG sample, the small grains were apparently undeformed. Only the larger grains were deformed, but not all of them. In Fig. 2c, it is apparent that most of the grains were undeformed, with grain II taking up most of the deformation. In some cases, the majority of a large grain remained undeformed, with the deformation limited to a single kink boundary (e.g. grain I in Fig. 2b).

5. Summary and conclusions

Based on the results presented here, the high temperature tensile creep deformation of fine- and coarse-grained Ti_3SiC_2 occurs by the formation of triple point cavities and plastic deformation of individual grains. At least three different plastic deformation mechanisms of individual grains were identified: (1) basal plane dislocation glide, (2) formation of dislocation walls of opposite sign, viz. kink boundaries, that result in multiple kinking of individual grains and, (3) formation of dislocation walls of the same sign that result in bending of grains or parts thereof. The deformation, especially, of the CG samples is also quite non-uniform.

Which mechanism(s) dominates in a particular grain, depends on the grain orientation relative to the applied load, its size, and more importantly, the local stresses that are highly inhomogeneous because of plastic anisotropy.

Appendix A.

A.1. Estimation of the normal and shear stresses in bent grains

The normal and shear stresses in the bent grains, shown in Figs. Fig. 6b and Fig. 8, were calculated using the following equations for the elastic bending of a beam:

$$\sigma = -E\frac{y}{\rho} \tag{1}$$

$$\tau = G\frac{dy}{dx} \tag{2}$$

Table A.1
Summary of various measurements of radii of curvature and resulting stresses.

	Δy (nm)	Δx (nm)	ρ (nm)	y (nm)	σ (Eq. (1)) (GPa)	τ (Eq. (2)) (GPa)
CG, Fig. 6b	28.6	274	1326	289 (Fig. 6b)	54	15
FG, Fig. 8d	4.3	38	162	10 (assumed)	23	17

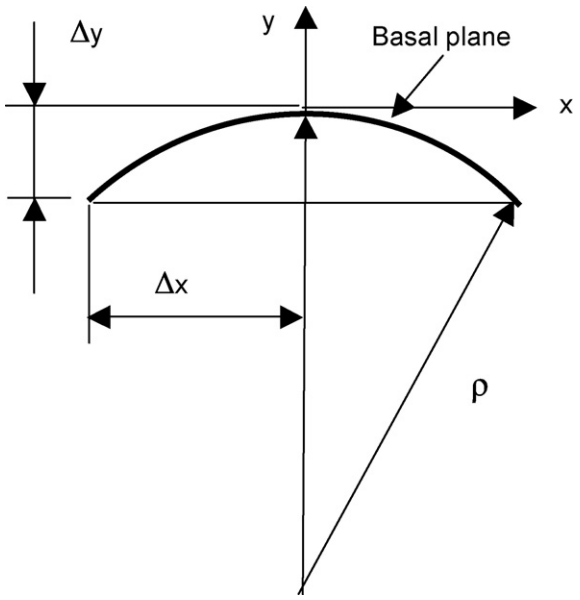

Fig. A.1. Schematic of geometrical distances assumed to estimate the normal and shear stresses (see text).

where σ and τ are the normal and shear stresses respectively; E and G are the Young's and shear moduli, respectively. The radius of curvature, ρ, and the distance from the neutral axes, y, are both defined in Fig. A.1. For Ti_3SiC_2 $E = 343$ GPa and $G = 143$ GPa [35]. The radius of curvature was estimated assuming:

$$\rho = \frac{(\Delta y)^2 + (\Delta x)^2}{2 \cdot \Delta y} \quad (3)$$

where Δx and Δy are defined in Fig. A.1. Radiuses of curvature for both CG and FG structure are determined from Figs. Fig. 6b and Fig. 8, respectively. For $\rho \gg \Delta y$, we can assume ρ is constant and does not change along the thickness of the grain, and that $dx = \Delta x$ and $dy = \Delta y$. For the CG microstructure, y is assumed to be equal to half of the thickness of the bent ribbon in Fig. 6b, In the case of the FG microstructure, it was assumed, conservatively, that y was equal to the thickness of area B visible in Fig. 8d. The calculation results are shown in Table A.1.

References

[1] M.W. Barsoum, T. El-Raghy, J. Am. Ceram. Soc. 79 (1996) 1953–1956.
[2] M.W. Barsoum, T. Zhen, S.R. Kalidindi, M. Radovic, A. Murugahiah, Nat. Mater. 2 (2003) 107–111.
[3] D. Chen, K. Shirato, M.W. Barsoum, T. El-Raghy, R.O. Ritchie, J. Am. Ceram. Soc. 84 (2001) 2914–2920.
[4] C.J. Gilbert, D.R. Bloyer, M.W. Barsoum, T. El-Raghy, A.P. Tomasia, R.O. Ritchie, Scripta Mater. 238 (2000) 761–767.
[5] L. Farber, I. Levin, M.W. Barsoum, Phil. Mag. Lett. 79 (1999) 163–170.
[6] M.W. Barsoum, L. Farber, T. El-Raghy, I. Levin, Met. Mater. Trans. 30A (1999) 1727–1738.
[7] M.W. Barsoum, Prog. Solid State Chem. 28 (2000) 201–281.
[8] M.W. Barsoum, T. El-Raghy, Met. Mater. Trans. 30A (1999) 363–369.
[9] T. El-Raghy, M.W. Barsoum, A. Zavaliangos, S.R. Kalidindi, J. Am. Ceram. Soc. 82 (1999) 2855–2860.
[10] T. El-Raghy, M.W. Barsoum, J. Am. Ceram. Soc. 82 (1999) 2849–2854.
[11] M.W. Barsoum, L.H. Ho-Duc, M. Radovic, T. El-Raghy, J. Electrochem. Soc. 150 (2003) B166–B175.
[12] J. Wang, Y.C. Zhou, Annu. Rev. Mater. Res. 39 (2009) 10.1–10.29.
[13] H.B. Zhang, Y.W. Bao, Y.C. Zhou, J. Mater. Sci. Technol. 25 (2009) 1–38.
[14] M.W. Barsoum, in: K.H.J. Buschow, R.W. Cahn, M.C. Flemings, E.J. Kramer, S. Mahajan, P. Veyssiere (Eds.), Encyclopedia of Materials Science and Technology, Elsevier, Amsterdam, 2006.
[15] M.W. Barsoum, T. El-Raghy, L. Ogbuji, J. Electrochem. Soc. 144 (1997) 2508–2516.
[16] H. Zhang, Z.G. Wang, Q.S. Zang, Z.F. Zhang, Z.M. Sun, Scripta Mater. 49 (2003) 87–92.
[17] M.W. Barsoum, M. Radovic, in: K.H.J. Buschow, R.W. Cahn, M.C. Flemings, E.J. Kramer, S. Mahajan, P. Veyssiere (Eds.), Encyclopedia of Materials Science and Technology, Elsevier, Amsterdam, 2006.
[18] B.J. Kooi, R.J. Poppen, N.J.M. Carvalho, J.T.M. De Hosson, M.W. Barsoum, Acta Mater. 51 (2003) 2859–2872.
[19] E.J. Freise, A. Kelly, Proc. Phys. Soc. A 264 (1961) 269.
[20] T. El-Raghy, A. Zavaliangos, M.W. Barsoum, S.R. Kalidindi, J. Am. Ceram. Soc. 80 (1997) 513–516.
[21] F.C. Frank, A.N. Stroh, Proc. Phys. Soc. 65 (1952) 811–822.
[22] M.W. Barsoum, T. Zhen, A. Zhou, S. Basu, S.R. Kalidindi, Phys. Rev. B 71 (2005) 134101.
[23] A.G. Zhou, M.W. Barsoum, S. Basu, S.R. Kalidindi, T. El-Raghy, Acta Mater. 54 (2006) 1631–1639.
[24] A.G. Zhou, B. Basu, M.W. Barsoum, Acta Mater. 56 (2008) 60–67.
[25] J.B. Hess, C.S. Barrett, Trans. AIME 185 (1949) 599–606.
[26] T. Zhen, M.W. Barsoum, S.R. Kalidindi, Acta Mater. 53 (2005) 4163–4171.
[27] M.W. Barsoum, M. Radovic, P. Finkel, T. El-Raghy, Appl. Phys. Lett. 79 (2001) 479–481.
[28] M. Radovic, M.W. Barsoum, T. El-Raghy, S.M. Wiederhorn, Acta Mater. 49 (2001) 4103–4112.
[29] M. Radovic, M.W. Barsoum, T. El-Raghy, S.M. Wiederhorn, J. Alloys Compd. 361 (2003) 299–312.
[30] T. Zhen, M.W. Barsoum, S.R. Kalidindi, M. Radovic, Z.M. Sun, T. El-Raghy, Acta Mater. 53 (2005) 4963–4973.
[31] M. Radovic, M.W. Barsoum, T. El-Raghy, S.M. Wiederhorn, W.E. Luecke, Acta Mater. 50 (2002) 1297–1306.
[32] F.E. Hauser, C.D. Starr, L. Tietz, J.E. Dorn, Trans. Am. Soc. Metals 47 (1955) 102.
[33] A. Zhou, M.W. Barsoum, Metal. Mater. Trans. 40A (2009) 1741–1756.
[34] X.Y. Yang, H.M. Miura, T. Sakai, Mater. Trans. 44 (2003) 197–203.
[35] M. Radovic, A. Ganguly, M.W. Barsoum, T. Zhen, P. Finkel, S.R. Kalidindi, E. Lara-Curzio, Acta Mater. 54 (2006) 2757–2767.